RESEARCH ARTICLE | MARCH 07 2025

Framework for generating high-resolution Hong Kong local climate projections to support building energy simulations

Jiayao Wang (王佳瑶) ; Binura J. Kudagama ; Udara S. Perera ; Sunwei Li (李孙伟) ; Xuelin Zhang (张雪琳)

Physics of Fluids 37, 037126 (2025)
https://doi.org/10.1063/5.0254669

Physics of Fluids ARTICLE pubs.aip.org/aip/pof

Framework for generating high-resolution Hong Kong local climate projections to support building energy simulations

Cite as: Phys. Fluids **37**, 037126 (2025); doi: 10.1063/5.0254669
Submitted: 24 December 2024 · Accepted: 23 January 2025 ·
Published Online: 7 March 2025

View Online Export Citation CrossMark

Jiayao Wang (王佳瑶),[1] Binura J. Kudagama,[2] Udara S. Perera,[3] Sunwei Li (李孙伟),[4,a)] and Xuelin Zhang (张雪琳)[5,a)]

AFFILIATIONS

[1]Department of Civil and Environmental Engineering, The Hong Kong Polytechnic University, Hung Hom, Kowloon, Hong Kong
[2]Department of Civil & Environmental Engineering, Louisiana State University, Baton Rouge, Louisiana 70803, USA
[3]Department of Civil Engineering, Sri Lanka Institute of Information Technology, Malabe, Sri Lanka
[4]Shenzhen International Graduate School, Tsinghua University, Shenzhen, Guangdong, China
[5]School of Atmospheric Sciences, Sun Yat-san University, Zhuhai, China

[a)]**Authors to whom correspondence should be addressed:** li.sunwei@sz.tsinghua.edu.cn and zhangxlin25@mail.sysu.edu.cn

ABSTRACT

Finer resolution climate model projections are essential for designing regional building energy consumption and adaptation strategies under changing climate conditions. However, projections from Global Climate Models (GCMs) are typically coarse in resolution and subject to biases and uncertainty. To address this, the present study uses bilinear interpolation and morphing statistical downscaling to obtain high spatial (around 10 km) and temporal (hourly) resolution weather data, for more accurate estimations of future residential building energy consumption under climate change. An empirical quantile mapping bias-correction technique is applied to adjust the projection data from 44 GCMs under four representative Shared Socioeconomic Pathways (SSPs): SSP1-2.6, SSP2-4.5, SSP3-7.0, and SSP5-8.5. The bias-corrected data are validated against meteorological observations from the Hong Kong Observatory's King's Park station. The hourly data are then converted to typical meteorological year data and used as input for EnergyPlus to predict future energy consumption patterns in public rental housing in Hong Kong. Case studies under the four SSPs show that climate change will significantly impact residential building energy use. Energy consumption is projected to increase by up to 14.0% for harmony-type buildings, 12.8% for trident-type buildings, and 12.4% for slab-type buildings by the end of the century under the SSP5-8.5 scenario, highlighting the urgent need for adaptive building design and energy policy measures.

I. INTRODUCTION

Climate change poses the most significant threat to humanity especially in recent decades.[1] The latest Intergovernmental Panel on Climate Change (IPCC) Synthesis Report from the Sixth Assessment Report (AR6) indicates that net greenhouse gas emissions have continued to rise since 2010, with temperatures from 2011 to 2020 averaging 1.1 °C above pre-industrial (1850–1900) levels.[2–4] The worsening climate may cause the increase in building energy consumption that can further exacerbate the global warming.[5] Therefore, actions from the building sector to mitigate and adapt to climate change are crucial to reduce the building energy consumptions.

There are two categories of downscaling methods: dynamical downscaling and statistical downscaling. The dynamical downscaling approach employs physics-based climate models which are similar to Global Climate Models (GCMs), but these conduct at refined resolutions (e.g., normally 10 and 30 km).[6] As a trade-off for this higher resolution, these models (also called as the regional climate models) are restricted to smaller regional scales rather than the entire globe.[7–9] However, achieving finer resolutions requires more computational resources. In contrast, statistical downscaling, with its relatively low computational requirements, provides a practical method for connecting local-scale variables with larger-scale atmospheric conditions.[9] The statistical downscaling method is adopted in this study due to its simple and relatively low computational consumptions. The statistical downscaling method includes the morphing method, which aims to apply the low-temporal resolution (e.g., monthly or daily) time series

of changes projected by GCMs onto high temporal resolution (e.g., hourly) baseline weather data by shifting, stretching, or a combination of the two;[10,11] regression method which aims to identify the statistical relationships between large-scale climate variables and regional-scale variables based on data mining;[12,13] and stochastic weather generators.[14,15]

With the hourly weather data incorporating climate change effects, researchers are able to evaluate the specific impacts of climate change on building energy consumption. Wang and Chen[16] adopted the HadCM3 GCM to project future climate change for three different CO_2 emission scenarios from IPCC AR4 and compared the climate change impacts on residential and commercial buildings energy consumptions in the U.S. Shibuya and Croxford[17] investigated the cooling and heating loads for office buildings in Japan through the A2 emission scenario from IPCC AR4 and demonstrated that the office buildings in Japan have significant potentials to reduce energy requirements. The same climate change scenarios from IPCC AR4 were also adopted by Shen and Lior,[18] Jentsch *et al.*,[19] and Shen.[20] Hwang *et al.*[21] quantified the climate change impacts on building envelop energy conservation index for office buildings in Taiwan through the Representative Concentration Pathway 4.5 (RCP4.5) from IPCC AR5 via the CanESM2 GCMs. Liu *et al.*[5] ensembled 24 GCMs in RCP4.5 and RCP8.5 from IPCC AR5 to obtain the future weather data and employed the weather data in the building energy simulation to evaluate the impacts of future climate change. The studies, such as Cellura *et al.*,[22] Zhai and Helman,[23] and Chai *et al.*,[24] also adopted the RCPs climate change scenarios to project future weather data and estimate the building energy used. The IPCC has highlighted that no single model can provide the best projection because different GCMs have varied biases. Therefore, it is essential to use results from multiple models rather than relying on a single model to address the uncertainties inherent in GCMs.[25–27] Many previous studies have limited their research to only a small number of models and scenarios or have used a single model with multiple scenarios. This approach can restrict the robustness and applicability of the findings, as it may not adequately capture the range of possible climate futures. In addition, many previous studies on the impact of climate change on building energy consumption have relied on outdated IPCC scenarios, such as AR4 and AR5, rather than the latest AR6 scenarios which incorporate the more comprehensive Shared Socioeconomic Pathways (SSPs). This reliance potentially limits the relevance of these studies' findings to future conditions, as the newer scenarios reflect updated scientific and socioeconomic developments. Additionally, these studies often apply broad regional projections without considering the unique microclimatic conditions of specific locales. Such generalizations can lead to inaccuracies in climate impact projections and building performance simulations, especially in areas where local geography or urban density significantly influences climate conditions.

IPCC published the latest generation of climate change scenario—the Shared Socioeconomic Pathways (SSPs), which projects global socioeconomic changes with a set of climate policies,[2] varying from SSP5-8.5 (the severe pathway, ongoing fossil-fuel development) to SSP1-1.9 (sustainable pathway, with low challenges to mitigation and adaptation) for quantifying the global warming degrees, to describe the evolution of society and ecosystems until the end of this century.[2,28] In the framework of the Coupled Model Intercomparison Project Phase 6 (CMIP6), Global Climate Models (GCMs) are employed to simulate the climate response to various factors.[28,29] When assessing future building energy performance using GCM projections, three main challenges arise: (1) The inherent bias in GCMs which often shows significant differences between historical GCM outputs and observed weather data. (2) The coarse temporal resolution of GCM weather data do not satisfy the hourly resolution requirements of building energy simulations.[30–32] (3) The coarse spatial resolutions of GCMs can lead to inaccuracies when comparing model data to weather observations at specific locations.[33] Furthermore, the GCMs have substantial uncertainties including internal climate variability due to natural fluctuations over time, the use of different climate models that predict varied climate changes, and the uncertainty in future climate change pathways.[33] Therefore, this study aims to address these limitations and eliminate the uncertainties by obtaining the bias-corrected (BC), refined hourly future weather data in four climate change scenarios.

The present study provides a comprehensive framework for generating high-resolution projected weather data and integrating it into energy simulations for residential buildings in Hong Kong. Several key contributions make this study particularly valuable:

- Utilization of the latest climate change scenarios and all accessible GCMs: One of the key contributions of this research is devoted to adopting the latest version of climate change scenarios—SSPs (SSP1-2.6, SSP2-4.5, SSP3-7.0, and SSP5-8.5) and ensembled all accessible GCMs (44 in total) to obtain the projected future weather data, to fill the gap in the availability of high-resolution, location-specific climate data for energy simulation.
- Development of finer temporal and spatial resolution downscaled weather data: One of the main challenges in climate research is the lack of a unified gridded system to obtain the hourly weather data for building energy simulations. This study bridges that gap by using downscaling techniques (i.e., bilinear interpolation and morphing method) to convert coarse monthly data from 44 GCMs into hourly weather data with a higher spatial resolution of $0.1° \times 0.1°$ for longitude and latitude ($\sim$10 km), offering the accurately located and finer resolution weather data for energy estimation.
- A dual bias-correction technique to improve data accuracy: Two different bias-corrected methods are used for historical/observed data bias-correction [empirical quantile mapping method (EQM)] and projection data bias-correction (delta method of empirical quantile mapping) in the present study to mitigate the uncertainties in GCMs.

Following the downscaling of future monthly climate projections to hourly data, four future hourly datasets are created under the four SSPs from 2015 to 2100. These hourly weather files will be further divided into three time periods as 2015–2044, 2045–2074, and 2075–2100 to represent the near future, mid-century future, and far future for the analysis purposes, which shows the gradual changes of future climate and the variation impacts on future building energy consumptions. A Typical Meteorological Year (TMY) dataset is created for each dataset to represent each time period and future climate scenarios. Finally, the 12 TMY datasets (i.e., four SSPs with three time periods) are converted to EnergyPlus Weather (EPW) files to be used in building energy simulations for a tall building located in Hong Kong to discuss the climate change impacts on energy consuming.

After the introduction, Sec. II articulates the method for projected future weather data downscaling and bias-correction, and also illustrates how to build the TMY dataset. Section III presents the validation of the bias-corrected data with the overstating from metrological stations in Hong Kong and discussed the building energy consumption results under different future climate conditions. Finally, concluding remarks are given in Sec. IV.

II. METHOD

The method revolves around assessing future building energy consumption based on climate model projections (as shown in Fig. 1). Initially, GCMs provide macro-scale climate data, which is then statistically downscaled to generate finer resolution future climate data. In the second step, the downscaled data are used to do the multi-model ensemble (MME) and bias-correction, then do the TMY data selection to prepare inputs that are specific for building energy consumption in Hong Kong under changing climate. These inputs are crucial for evaluating the energy use intensity (EUI), which involves analyzing various energy demands, such as lighting, heating, cooling, and equipment usage in buildings. Ultimately, future building energy use intensity will link climate change impacts directly with energy consumption scenarios in built environments.

A. Building energy simulations

EnergyPlus software is adopted to assess the future energy performance of buildings in Hong Kong for the present study. EnergyPlus utilizes full-year weather data in the EPW format, which incorporates multiple weather parameters at hourly intervals for simulation. Developed by Crawley *et al.*,[34] the EPW file format and its critical weather parameters have become the standard for many building simulation tools. Ten essential weather parameters are needed to be extracted from the GCMs to compose EPW files, which include dry bulb temperature (DBT), dew point temperature, relative humidity (RH), atmospheric pressure (AP), horizontal infrared radiation intensity, direct normal radiation, diffuse horizontal radiation, wind direction, wind speed, and total sky cover (TSC).[5,35] The aforementioned EPW weather data are extracted from multiple GCMs according to the availability. Additionally, some essential weather parameters are not directly obtainable from the GCMs; instead, they are derived using

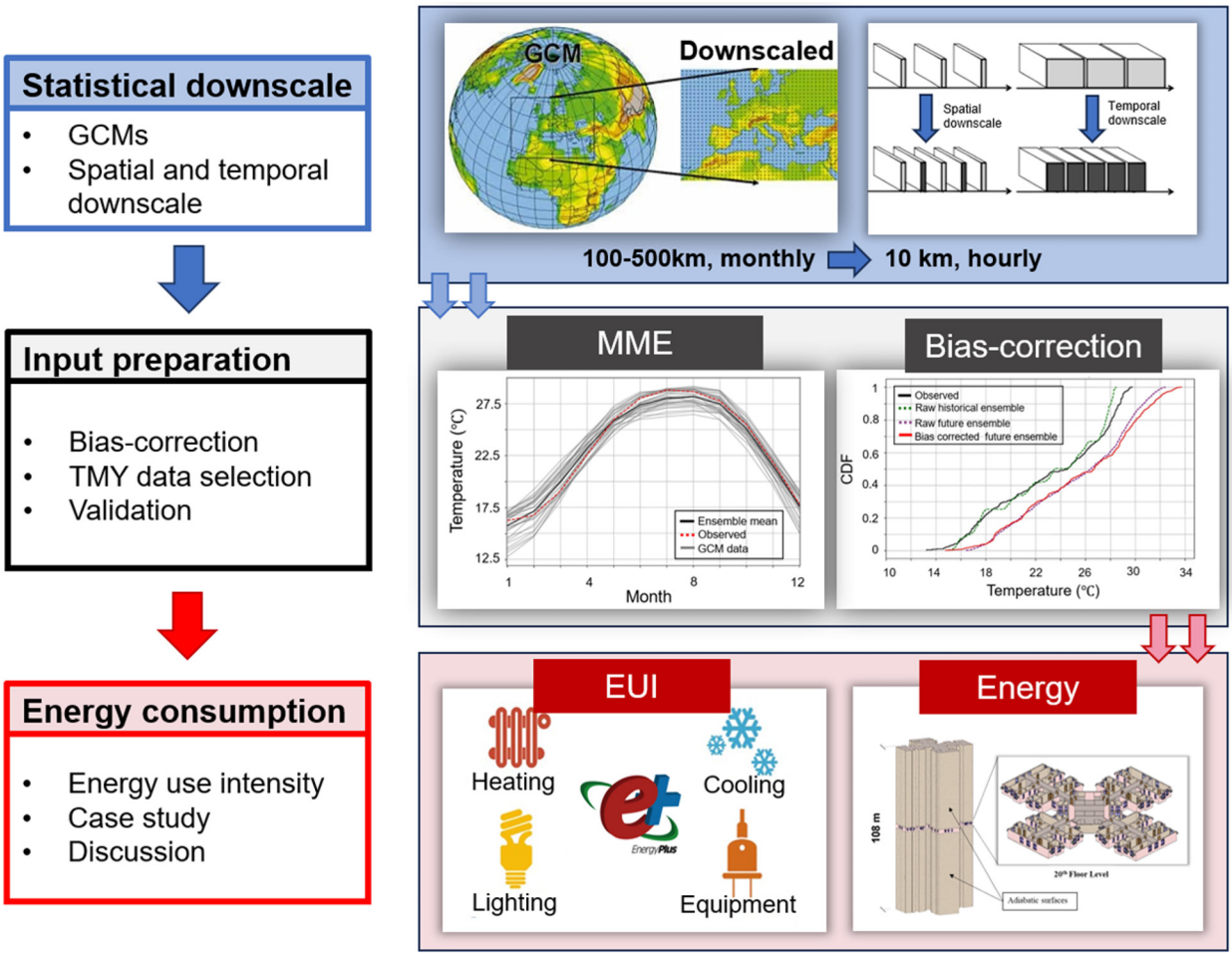

FIG. 1. The method flow chart.

existing weather data according to methods illustrated in Sec. II E and Table II. In general, an EPW file containing 8760 (24 h × 365 days) hourly records of ten essential climate variables is required for a building energy simulation.[36] However, the accessible GCMs often offer daily or monthly weather data which require downscaling techniques to derive the required hourly data for accurate building energy simulations. The details on downscaling method are presented in Sec. II E. EnergyPlus calculates energy demand for heating and cooling systems (E_{hvac}) based on load due to heat transfer between indoor spaces and outdoors and indoor heat generation. In addition, the energy demand for lighting ($E_{lighting}$) and equipment ($E_{equipment}$) are calculated based on the lighting and equipment schedule and its intensities. The operational energy of the building is subsequently normalized per unit floor area, referred to as EUI, of the building according to Eq. (1), the unit is kWh/m^2.

$$Operational\ Energy\ (EUI) = \frac{\sum (E_{hvac} + E_{lighting} + E_{equipment})}{Total\ floor\ area}. \quad (1)$$

B. Climate variables and GCMs

The CMIP6 consists of around 133 GCMs (e.g., ACCESS-CM2, BCC-CSM2-MR, CanESM5, and CESM2) from 49 modeling centers (e.g., Commonwealth Scientific and Industrial Research Organization from Australia, Beijing Climate Center from China, Canadian Center for Climate Modeling and Analysis from Canada, and National Center for Atmospheric Research from the U.S.). The GCMs under CMIP6 typically feature gridded data with varying grid systems and spatial resolutions (e.g., 100, 250, and 500 km), with different temporal resolutions (e.g., daily and monthly).

The selection of model data for both historical (1981–2014) and future (2015–2100) climate projections is guided by the availability of GCMs concerning required climate variables, experiments, and temporal resolutions. The goal is to gather the highest possible number of GCMs for each climate variable under each SSP scenario. Nonetheless, due to constraints in data availability, it is impractical to maintain a consistent number of GCMs for each climate variable across historical and SSP scenarios (SSP1-2.6, SSP2-4.5, SSP3-7.0, and SSP5-8.5). Consequently, a decision was made to proceed with a variable yet significant number of models, ensuring a minimum collection of 15 GCMs for each climate variable. In total, 44 different GCMs were considered in the collection process under nine climate variables (details can be found in Appendix Tables VII and VIII). Table I details the climate variables from GCM collection along with their abbreviations and the corresponding EPW climate variables. Five climate change pathways—historical, SSP1-2.6, SSP2-4.5, SSP3-7.0, and SSP5-8.5—are included in the collection of modeled data for each climate variable. Although there is no widely accepted "best performing" GCM, the selected models are widely recognized in climate modeling research and have demonstrated reliability in prior studies.[26,37]

C. Multi-model ensembles

Numerous studies have utilized MME techniques to diminish simulation uncertainty and enhance the reliability of future climate projections derived from GCMs.[1,38,39] There are two primary MME approaches documented: (1) computing the mean value from a set of GCMs and (2) calculating a weighted average for GCMs by assigning varying weight factors to the considered models.[40] The present study chooses the first method to average climate variables from multiple GCMs to derive the MME mean due to its simplicity and computational efficiency. This straightforward approach requires less computational power compared to more complex weighting schemes, ensuring both transparency and ease of replication for verification. The ensemble mean was computed by averaging all the gathered raw GCM data from historical and future SSPs for each climate variable, with each model weighted equally. The MME mean can be computed using Eq. (2), where n is the total number of GCMs collected for each climate variable, $GCM(x_i)$ is the output variable of the ith GCM, and $[\sum_{i=1}^{n}]$ represents the sum of the outputs of all the GCMs considered.

$$MME = \frac{1}{n}\sum_{i=1}^{n} GCM(x_i). \quad (2)$$

D. Bias-correction method

Due to their low spatial resolution, GCM data often fail to capture regional and local features, such as vegetation and topography. This limitation can lead to significant differences when comparing historical GCM data with observed data from local metrological stations over the same period.[31] A well-accepted hypothesis in climate model evaluation is that the biases observed between historical model data and observation weather data are likely to persist in future climate projections.[41,42] Consequently, the existing biases in the present are expected

TABLE I. Essential climate variables collected from GCMs for EPW data preparation.

Climate variable	Acronym	Units	EPW climate variable
Near-surface air temperature	tas	°C	Dry bulb temperature (°C)
Minimum near-surface air temperature	tasmin	°C	
Maximum near-surface air temperature	tasmax	°C	
Near-surface relative humidity	hurs	···	Relative humidity (%)
Air pressure at mean sea level	psl	Pa	Atmospheric pressure (Pa)
Surface downwelling shortwave flux in the air	rsds	W/m^2	Global horizontal irradiance (Wh/m^2)
Eastward wind speed	uas	ms^{-1}	Wind speed (ms^{-1})
Northward wind speed	vas	ms^{-1}	
Cloud area fraction	clt	%	Total sky cover (tenths of sky)

to be mirrored in future climate scenarios. Addressing these biases is essential for accurate climate impact assessments. Therefore, in this study, a dual bias-correction technique is adopted to get the ensemble means of each climate variable—both historical and future—are adjusted to mitigate their inherent biases within the GCMs. This calibration ensures that the model outputs are more representative and reliable for projecting future climate conditions.

There are many bias-correction approaches developed to provide more realistic future climate projections. A common method used for bias-correction is empirical quantile mapping (EQM), which has been proven to effectively mitigate certain biases in GCMs while demanding minimal computational resources.[43,44] The basic principle in the EQM method is to establish a statistical relationship between observed weather data and historical model data and then apply the established transfer function to future model projections.[45] The EQM method uses Cumulative Distribution Functions (CDFs) to map the distribution of monthly GCM climate variables onto that of observed weather data.[46] The current study uses this method to bias-correct historical model data with the observed data. This method can be expressed according to the following equation:[39]

$$x_{mh,corr} = F_{oh}^{-1}\left(F_{mh}\left(x_{mh,raw}\right)\right), \tag{3}$$

where $x_{mh,corr}$ denotes the bias-corrected historical-modeled data, $x_{mh,raw}$ is the raw historical-modeled data, F_{oh}^{-1} is the inverse cumulative distribution of the historical observed data (x_{oh}), and F_{mh} is the CDF of the historical modeled data (x_{mh}). F is the CDF of either the observations (o) or model (m) for the historic period (h) or future projection period (f).

The EQM bias-correction for future model data is done by locating the corresponding percentile values for the future model data points in the CDF of the historical modeled data and then by locating the historical observed data for the same CDF values of the historical observed data. However, this approach relies on an assumption that the climate distribution remains relatively stable over time, implying that the variance and skew of the distribution remain constant while only the mean value changes.[45] This assumption might not always hold, as there is a possibility of significant changes in the climate distribution with the model simulations over time. Li *et al.*[45] introduced a novel approach termed as equidistant CDF matching method (EDCDFM) or the delta method of EQM to allow such changes. Here, the bias-correction is performed by integrating data from the CDF of the model projection, rather than presuming that the historical model distribution remains applicable to the future timeframe. The delta method of EQM [in (4)] is adopted to correct prediction data in this research, where the parameter definitions are the same as Eq. (2).

$$x_{mf,corr} = x_{mf,raw} + F_{oh}^{-1}\left(F_{mf}\left(x_{mf,raw}\right)\right) - F_{mh}^{-1}\left(F_{mf}\left(x_{mf,raw}\right)\right). \tag{4}$$

E. Downscaling methods

The bilinear interpolation method is one of the simplest downscaling techniques, utilizing linear interpolation based on distance.[32,47–50] It works by selecting the four nearest coarse grid points to the target grid, which has finer resolution, and then applying inverse distance-weighted interpolation. This method assumes that pixel intensity varies linearly across the image, and the pixel value $f(x,y)$ is computed using the values of the four surrounding pixels: $f(0,0)$, $f(1,0)$, $f(0,1)$, and $f(1,1)$, as shown in Eq. (5). In the context of GCMs, bilinear interpolation is employed to re-grid the model outputs to a higher spatial resolution of $0.1^\circ \times 0.1^\circ$ for both longitude and latitude (~10 km). This process unifies the various grid systems and resolutions used by different GCMs, allowing for more accurate localization of the study area (i.e., Hong Kong).

$$\begin{aligned} f(x,y) = {} & f(0,0)(1-x)(1-y) + f(1,0)x(1-y) \\ & + f(0,1)(1-x)y + f(1,1)xy. \end{aligned} \tag{5}$$

Morphing method is a widely accepted temporal downscaling method which including three generic algorithms to shift, stretch, and combine the shift and stretch together, to temporally downscale the low resolution (i.e., monthly in this study) climate variables to high resolutions (i.e., hourly in the present research).[5,11] The algorithms are presented in Eqs. (6)–(10):

- A shift of Δx_m is applied to the baseline hourly climate variable x_0 by

$$x = x_0 + \Delta x_m. \tag{6}$$

  Here, the Δx_m is the shifting factor which is the absolute change in monthly mean values between future model data and baseline climate data (TMY data) of a certain climate variable for the month m. A shift is applied when an absolute change to the future mean value of a certain variable is required, while maintaining the monthly variance unchanged. The shifting factor Δx_m can be calculated as typically expressed in the following equation:

$$\Delta x_m = \langle x_{model} \rangle_m - \langle x_0 \rangle_m. \tag{7}$$

- A stretch of α_m is applied to the baseline hourly climate variable x_0 by

$$x = \alpha_m x_0. \tag{8}$$

  Here, α_m is the stretching factor which is the fractional change between future model data and baseline climate data (TMY data) of a certain variable for month m. A stretch is used when a change in future monthly mean and variance of the climate variable is required as a fractional change rather than an absolute change. The stretching factor α_m can be calculated as typically expressed in the following equation:

$$\alpha_m = \frac{\langle x_{model} \rangle_m}{\langle x_0 \rangle_m}. \tag{9}$$

- A combination of shift and stretch is applied to the baseline hourly climate variable x_0 by

$$x = x_0 + \Delta x_m + \alpha_m\left(x_0 - \langle x_0 \rangle_m\right). \tag{10}$$

  This algorithm is applied when there is a requirement to change the future monthly mean and variance of the climate variable. For example, the combination algorithm is adopted for the downscaling of dry bulb temperature to reflect changes in mean, maximum, and minimum dry bulb temperatures. Table II illustrates the details of the essential EPW weather variables, projected climate variables from GCMs relevant to the EPW weather variable, and the method/algorithm used for the generation of future hourly weather data along with the shifting and stretching factor used for the relevant parameters.

In addition to the EPW variables discussed in Table II, another essential weather parameter called horizontal infrared radiation intensity was derived using the following equations developed by Walton[51] using the other downscaled weather parameters in the following equation:

$$Horizontal_{IR} = \epsilon\sigma T_{drybulb}^4, \tag{11}$$

where $Horizontal_{IR}$ is the horizontal infrared intensity (W/m^2), ϵ is the sky emissivity, σ is the Steffan–Boltzmann constant which is $5.6697e^{-8} W/m^2K^4$, and $T_{drybulb}$ is the dry bulb temperature (K). The sky emissivity (ϵ) is given in Eq. (12), where $T_{dewpoint}$ is the dew point temperature (K), N is the sky cover (tenths).

$$\epsilon = \left(0.787 + 0.764\ln\left(\frac{T_{dewpoint}}{273}\right)\right) \times (1 + 0.0224N - 0.0035N^2 + 0.00028N^3). \tag{12}$$

After implementing three morphing algorithms, future hourly weather data were synthesized using the baseline climate represented by the historical TMY weather file. Subsequently, essential hourly EPW parameters were identified, leading to the creation of four distinct hourly datasets from 2015 to 2100 under SSP1-2.6, SSP2-4.5, SSP3-7.0, and SSP5-8.5. Each of these datasets comprised 753 360 time-steps and included ten corresponding EPW parameters. For analytical purposes, the projected hourly datasets were divided into three periods—2015–2044, 2045–2074, and 2075–2100—categorized as near future, mid-century future, and far future, respectively, for each SSP scenario. This division resulted in 12 datasets across the four SSPs and three time periods, specifically configured for future building energy simulations. Given that EnergyPlus software requires a representative year with hourly weather parameters for future time periods, 12 future TMY weather files were generated using the Sandia method. These TMY weather files were subsequently converted into the EPW file format to ensure their compatibility with EnergyPlus. Figure 2 illustrates the comprehensive method adopted in preparing aforementioned future

TABLE II. Morphed EPW weather variables along with climate projection parameters and an overview of the method used to generate future weather data.

EPW variable	Parameters from GCMs	Method/algorithm used to generate future hourly weather data	Shifting factor (Δx_m)	Stretching factor (α_m)
Dry Bulb Temperature (DBT, °C)	tas tasmin tasmax	Combination of shift and stretch $T = T_0 + \Delta T_m + \alpha_m(T_0 - \langle T_0\rangle_m)$	$\Delta T_m = \langle T_{model}\rangle_m - \langle T_0\rangle_m$	$\alpha_m = \frac{\Delta Tmax_{model,m} - \Delta Tmin_{model,m}}{\langle Tmax_0\rangle_m - \langle Tmin_0\rangle_m}$
Relative Humidity (RH, %)	Hurs	Stretch algorithm $RH = \alpha_m RH_0$	...	$\alpha_m = \frac{\langle RH_{model}\rangle_m}{\langle RH_0\rangle_m}$
Dew Point Temperature (DPT, °C)	...	Derived using downscaled DBT and RH values $DPT = DBT - \left(\frac{100 - RH}{5}\right)$	...	...
Atmospheric Pressure (AP, Pa)	psl	Shift algorithm $AP = AP_0 + \Delta AP_m$	$\Delta AP_m = \langle AP_{model}\rangle_m - \langle AP_0\rangle_m$	...
Global Horizontal Illuminance $\left(\text{GHI}, \frac{\text{Wh}}{\text{m}^2}\right)$	rsds	Stretch algorithm $\text{GHI} = \alpha_m GHI_0$	...	$\alpha_m = \frac{\langle GHI_{model}\rangle_m}{\langle GHI_0\rangle_m}$
Direct Normal Illuminance $\left(\text{DNI}, \frac{\text{Wh}}{\text{m}^2}\right)$	...	DNI is derived using a model called DIRINT developed by Perez *et al.* (1992). A python function is available in pvlib toolbox to perform DIRINT model	...	...
Diffuse Horizontal Illuminance $\left(\text{DHI}, \frac{\text{Wh}}{\text{m}^2}\right)$	...	Derived using the downscaled GHI, derived DNI, and solar zenith angle (θ_z) data. $GHI = DHI + DNI.\cos(\theta_Z)$	...	...
Wind Speed (WS, m/s)	uas vas	Stretch algorithm $\text{uas} = \alpha_m uas_0$ $\text{vas} = \alpha_m vas_0$ $WS = \sqrt{(uas)^2 + (vas)^2}$	...	$\alpha_m = \frac{\langle uas_{model}\rangle_m}{\langle uas_0\rangle_m}$ $\alpha_m = \frac{\langle vas_{model}\rangle_m}{\langle vas_0\rangle_m}$
Wind Direction (WD, °)	...	Derived using the tangent of downscaled *uas* and *vas*	...	...
Total Sky Cover (TSC)	clt	Shift algorithm $TSC = TSC_0 + \Delta TSC_m$	$\Delta TSC_m = \langle TSC_{model}\rangle_m - \langle TSC_0\rangle_m$	...

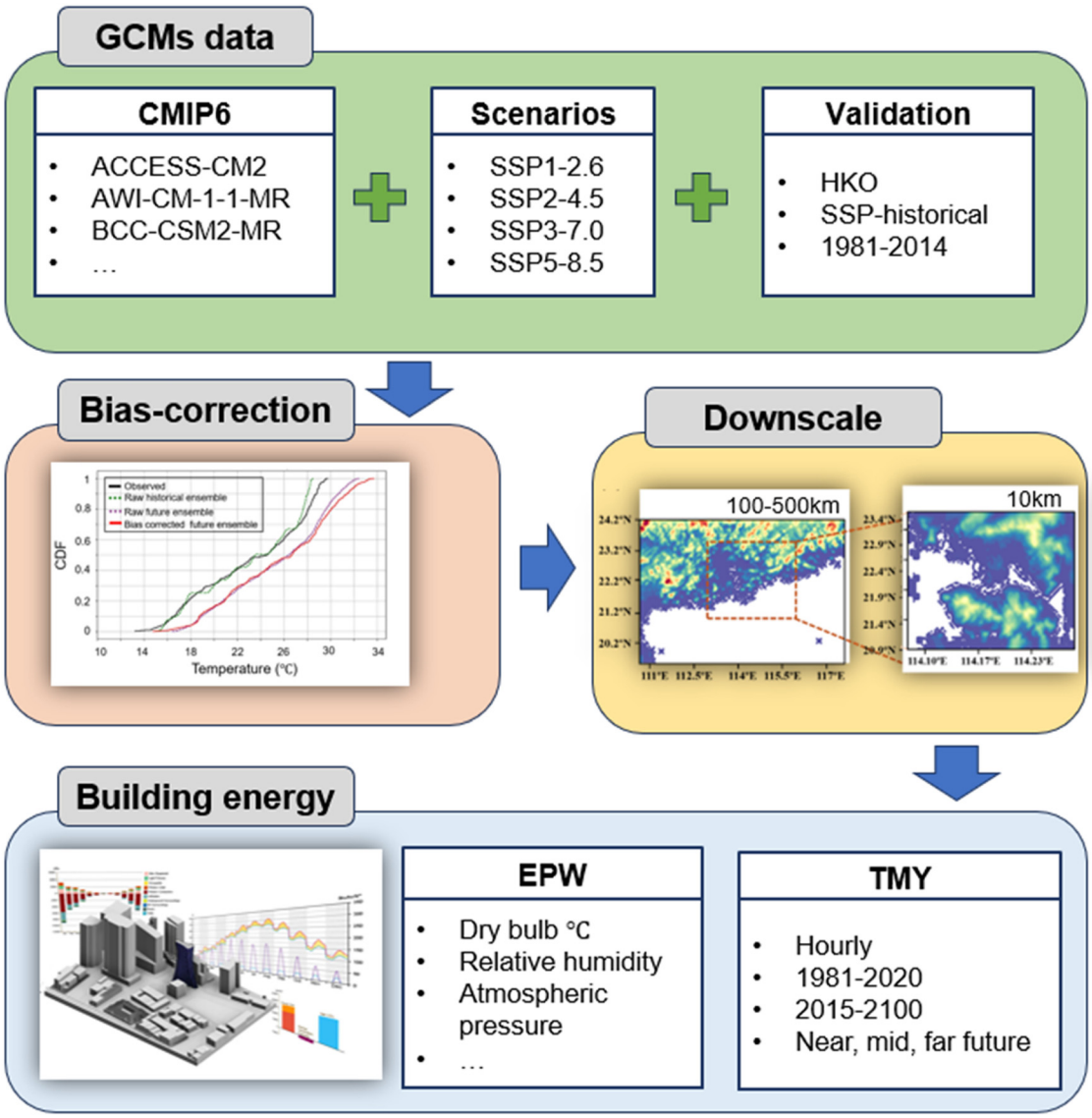

FIG. 2. Method for future weather dataset preparation and building energy simulation flow chart.

climate datasets and EPW files, which are utilized to conduct building energy simulations.

F. Typical metrological year

Due to the natural variability of climate systems, the weather for a typical location shows significant interannual variations.[2] Consequently, analyzing weather data from a single, arbitrary year may introduce substantial biases.[52,53] A common solution to this issue is the creation of representative year (i.e., TMY) that accurately reflect the long-term average characteristics of the local climate.[54,55] Therefore, a TMY weather dataset is developed using observed hourly meteorological data sourced from the Hong Kong Observatory (HKO) King's Park meteorological station from 1981 to 2020. The TMY dataset is constructed into an EPW file format following the Sandia Method, as detailed in Wilcox.[56] The construction of the TMY weather file involved a meticulous statistical analysis of nine daily-weather indices extracted from HKO King's Park hourly recordings. These indices include daily maximum, minimum, and mean dry bulb temperature, daily maximum, minimum, and mean dew point temperature, daily maximum and mean wind speed, and daily total global horizontal solar radiation.[35] Each of these indices was carefully analyzed to create a TMY weather file that effectively represents the baseline climate.

III. RESULTS AND DISCUSSION

A. Results of the MME

Figure 3 illustrates (a) the historical monthly mean and (b) the annual mean of near surface temperature from 1981 to 2014 as the

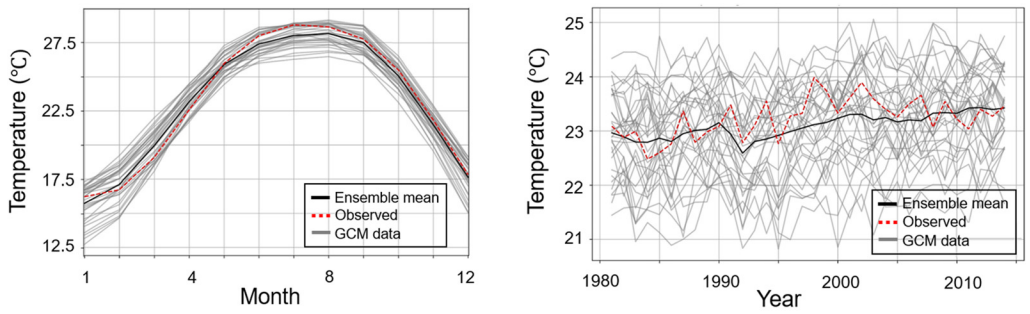

(a) Monthly mean (b) Annual mean

FIG. 3. Comparison of (a) monthly averaged and (b) annual averaged near surface temperature from observed data and modeled historical data along with their MME mean from 1981 to 2014.

example to illustrate the MME results. This analysis qualitatively evaluates the performance between the raw outputs of the GCMs MME mean, observed meteorological data, and historical weather data modeled by multiple GCMs. The gray lines shown in Fig. 3 correspond to the historical near surface temperature modeled from a collection of 32 GCMs (details can be found in Table VIII). Figure 3(a) presents a comparative analysis of monthly mean near surface temperatures from 1981 to 2014. The analysis generates the mean temperatures for each month by averaging observations/MME mean/individual GCMs from all months. The observed data series slightly exceeds the ensemble mean in January. However, from February through the end of the spring, the observed temperatures are consistently marginally lower than those of the ensemble mean. During the summer months (June to September), the observed temperatures are higher than those of the ensemble mean. Although both the observed and ensemble mean temperatures peak in July, the observed data align closer to the upper boundary of the 32 GCMs outputs. There is a pronounced alignment between the ensemble mean and observed data series in the autumn and winter months, demonstrating a high consistency in temperature measurements between the two datasets.

The annual near surface temperature in Fig. 3(b) illustrates a general upward trend for both the observed and ensemble mean data, with both datasets showing a similar long-term increasing trend indicative of gradual warming over the period. Interestingly, both the observed and ensemble mean data series show a decrease around 1992, indicating a synchronized low point. However, the variability between these two series is different, and the observed data illustrate more significant fluctuations. This is particularly evident that the observed data peak around 24 °C in 1998 and trough around 22.5 °C in 1984, highlighting greater extremes in the observed data compared to the ensemble mean. Regarding the outputs from the 32 individual GCMs, the figure shows a broad spread of annual mean temperatures ranging from approximately 21 °C to around 25 °C. This wide variance shows the inherent uncertainties present among the different GCMs, reflecting the diversity in model sensitivity and method. The considerable spread in the GCM outputs illustrates the reason why relying on a single GCM could be scientifically inadequate. Consequently, employing the MME is justified as it integrates across the varying outputs, thereby mitigating the potential errors associated with individual models and providing a more reliable and stable representation of climate trends.

Table III provides a detailed quantitative analysis utilizing the Pearson correlation coefficient (R), bias, and root mean square error (RMSE) values to assess the agreement between the monthly averaged historical near-surface temperature data observed from 1981 to 2014 and the outputs from 32 individual GCMs, as well as their MME means. The correlation coefficients for the individual GCMs range from 0.922 to 0.971, reflecting a generally high degree of linear agreement with observed temperatures. Models, such as BCC-CSM2-MR and TaiEMS1, show particularly strong correlations, with coefficients of 0.971 and 0.966, respectively, indicating their robust performance in capturing temperature trends. However, the Pearson correlation for the MME mean of these 32 GCMs is significantly higher at 0.977, which the correlation exceeds any single model, illustrating the enhanced reliability and accuracy of the MME method. The bias values indicate the systematic error in the model predictions. For instance, models, such as E3SM-2-0-NARRM and GFDL-ESM4, have large biases (−1.429 and −1.717, respectively), suggesting these models tend to underestimate the near-surface temperature significantly. The MME case has a bias of −0.15, indicating a slight overall underestimation of the temperature across the ensemble. In contrast, several GCMs' absolute bias values are slightly lower than the MME case, such as the BCC-CSM2-MR (−0.08), CAMS-CSM1-0 (−0.073), CESM2-FV2 (0.066), CMCC-CM2-HR4 (0.148), HadGEM3 (−0.121), INM-CM4-8 (0.014), and MRI-ESM2-0 (0.102). As for the root mean square error (RMSE), which reflects the overall deviation of the models' predictions from the observed values, models like BCC-CSM2-MR and TaiESM1 show relatively low RMSE values (1.139 and 1.264, respectively), suggesting good performance with minimal deviation from the observed temperatures. On the other hand, GFDL-ESM4 shows a significantly higher RMSE of 2.375, indicating that its predictions deviate more from the observed data. The MME model achieves the lowest RMSE of 1.04, highlighting that the ensemble method provides the most accurate and consistent results among all models. Therefore, the MME mean not only unifies the diverse outputs from the individual GCMs but also mitigates their individual biases and errors, resulting in a more consistent and accurate representation of historical temperature patterns. This finding demonstrates the application of MME mean in analyzing historical and projecting future SSPs for various climate variables. Therefore, the MME mean provides a more dependable basis for scientific assessments and policy formulations related to climate change.

TABLE III. Pearson correlation coefficient (R), bias, and root mean square error (RMSE) values for monthly averaged historical and observations of near surface temperature variables. "MME mean" denotes the multi-model ensemble mean.

GCM	R	Bias	RMSE	GCM	R	Bias	RMSE
AWI-CM-1-1-MR	0.945	0.843	1.767	E3SM-2-0-NARRM	0.960	−1.429	2.085
BCC-CSM2-MR	0.971	−0.080	1.139	EC-Earth3	0.958	−0.898	1.628
CAMS-CSM1-0	0.940	−0.073	1.621	EC-Earth3-AerChem	0.958	−0.926	1.660
CAS-ESM2–0	0.943	0.264	1.745	EC-Earth3-CC	0.954	−0.44	1.481
CESM2	0.957	0.760	1.562	EC-Earth3-Veg	0.953	−0.507	1.531
CESM2-FV2	0.946	0.066	1.541	FGOALS-f3-L	0.964	−0.744	1.456
CESM2-WACCM	0.959	0.703	1.513	FIO-ESM-2-0	0.963	0.837	1.563
CESM2-WACCM-FV2	0.952	0.303	1.498	GFDL-ESM4	0.951	−1.717	2.375
CIESM	0.958	1.059	1.748	HadGEM3	0.955	−0.121	1.534
CMCC-CM2-HR4	0.946	0.148	1.714	INM-CM4-8	0.922	0.014	2.028
CMCC-CM2-SR5	0.961	0.709	1.480	INM-CM5-0	0.939	−0.663	1.920
CMCC-ESM2	0.961	0.498	1.403	MPI-ESM1-2-HR	0.951	0.156	1.518
E3SM-1-0	0.955	−0.724	1.641	MRI-ESM2-0	0.959	0.102	1.385
E3SM-1-1	0.947	−1.281	2.093	NorESM2-MM	0.952	0.428	1.511
E3SM-1-1-ECA	0.954	−0.927	1.798	SAM0-UNICON	0.965	−0.228	1.267
E3SM-2-0	0.964	−1.177	1.866	TaiESM1	0.966	0.244	1.264
MME mean of 32 GCMs	**0.977**	−0.150	1.04				

B. Results of the bias-correction

The study employs the EQM method for the observed weather data bias-correction, while the delta method EQM is utilized for the bias-correction of future weather data projections. The approach facilitated the adjustment of the MME means for each climate variable for both historical and future datasets, enhancing the reliability of the model outputs. Figure 4 presents a case study of how the EQM method and the delta method of EQM are applied to correct the near surface temperature (tas) values. This figure illustrates the effectiveness of the EQM bias-correction across different datasets. The black solid line represents observed temperature data from 1981 to 2014 as the baseline. The green dashed line shows the raw historical ensemble mean, while the purple dashed line shows the raw future ensemble mean for the period 2015–2100 under the SSP5-8.5 scenario, and the red solid line indicates the bias-corrected ensemble for the same future period. Figure 4 clearly indicates that the bias-corrected future ensemble mean aligns more closely with the observed data than the uncorrected projections (raw future ensemble), substantiating the efficiency of the EQM method in adjusting future climate projections to reflect expected trend (similar to the historical trend) more accurately. Through these corrections, the ensemble means are calibrated to provide a more accurate forecast, mitigating potential misrepresentations and enhancing the model's applicability for future climate scenario assessments.

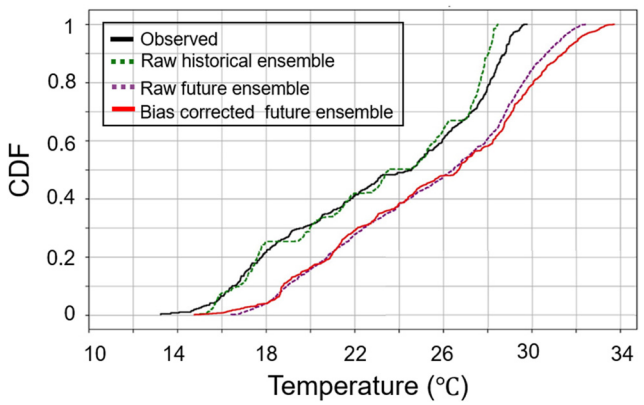

FIG. 4. Bias-correction of future climate projections using the near surface temperature dataset.

C. Weather data validation

After conducting the bias-correction, a validation test is generated to assess the reliability of various weather parameters as predicted by GCMs and to evaluate the efficacy of the bias-correction method employed. This validation utilized the most influential monthly observed weather data alongside historical raw GCM data (non-bias-corrected, NBC) and bias-corrected model data from 1981 to 2014. The assessment of the reliability of different weather parameters and the accuracy of the bias-correction method was carried out both quantitatively and qualitatively using Taylor diagrams, as introduced by Taylor.[57] Taylor diagrams provide a graphical representation that summarizes the quantification of similarity between two patterns through three statistical metrics: the Correlation Coefficient (R), centered Root-Mean-Squared Error (Centered RMSE), and Standard Deviation (SD). By integrating these three statistical measures into a single cohesive diagram, Taylor diagrams enable a comprehensive and comparative analysis of two time-series datasets, representing both observations and GCM outputs for Hong Kong.

Table IV and Fig. 5 present the results for a series of Taylor diagrams of various weather parameters that are the most influential to

TABLE IV. Performance of the delta method for EQM bias-correction and reliability of climate model data using standard deviation, centered RMSE, and correlation coefficient. NBC: non-bias-corrected; BC: bias-corrected.

		DBT	GHI	AP	RH	EWS	NWS	TSC
R	Observed	1	1	1	1	1	1	1
	NBC	0.9769	0.644	0.970	0.699	0.678	0.729	0.397
	BC	0.9766	0.630	0.962	0.644	0.645	0.691	0.471
Centered RMSE	Observed	0	0	0	0	0	0	0
	NBC	1.029	29.868	138.347	4.403	0.941	2.073	1.207
	BC	1.019	29.884	156.846	5.078	0.853	0.485	1.294
SD	Observed	4.723	34.934	567.091	6.059	1.016	0.620	1.268
	NBC	4.410	35.956	559.325	5.028	1.262	2.484	0.830
	BC	4.703	34.608	565.154	5.988	1.012	0.615	1.251

the energy consumptions, including DBT, GHI, RH, AP, EWS, NWS, and TSC. These diagrams facilitate a comparison among monthly observed weather data, historical raw model data (non-bias corrected) and historical bias-corrected model data from 1981 to 2014. Each diagram incorporates the observed as the reference case, with the centered RMSE represented by blue dashed lines. Table IV provides a detailed quantitative evaluation of the delta method utilized for EQM bias-correction across various weather parameters. The table systematically presents the performance metrics for both non-bias-corrected (NBC) and bias-corrected (BC) climate model outputs compared to observed data for each parameter from 1981 to 2014.

The R values in Table IV reflect the degree of linear relationship between the model outputs and observed data (reference case), with higher values indicating better model performance. As shown, the R for DBT in NBC models is the highest ($R = 0.9769$) and slightly increased after bias-correction ($R = 0.9766$). TSC has the lowest R value for NBC case which is 0.397, then increase to 0.471 after the bias-correction. However, for other parameters like GHI and AP, the correlation slightly decreases post-correction, but the decline remains insignificant (all within an acceptable range of approximately 0.8%–7.7%), which does not dramatically impact the overall effectiveness of the models. The centered RMSE in Table IV, which measures the average magnitude of the error between predicted and observed values, with lower values indicating better model performance. After conducting the bias-correction, improvements in the centered RMSE are evident for certain parameters, such as DBT, EWS, and NWS. Specifically, the centered RMSE for NWS shows the most significant reduction, decreasing from 2.073 to 0.485, which represents a decrease in approximately 76.6%. This substantial reduction highlights the effectiveness of the bias-correction in improving the accuracy of wind speed predictions. Conversely, for other parameters, such as GHI, AP, and RH, the centered RMSE values have slightly increased, indicating a reduction in prediction accuracy following bias-correction. These increases vary (from 0.05% to 15.3%), with RH showing the largest rise in centered RMSE from 4.403 to 5.078 (15.3%). This increase suggests a decrease in the model's accuracy for RH post-correction, highlighting areas where the bias-correction method may require further refinement to enhance predictive reliability. The SD values in Table IV, which indicate the spread of the data points around the mean, generally remain consistent before and after bias-correction, suggesting that the variability in model outputs is preserved relative to the observed variability. For instance, in the case of BS, the SD values are noted to be closer to the observed data, with changes ranging from as minor as approximately 0.3% for AP (decreasing from 567.091 to 565.154) to about 1.3% for TSC (reducing from 1.268 to 1.251). In contrast, the NBC generally show larger deviations in SD from the observed values, with variations ranging between 1.4% and 300.6%. This is particularly evident in NWS, where the NBC model's SD deviate is 2.484 compared with the observed SD which is 0.620 (300.6%), illustrating a greater disparity in variability between the NBC models and actual observed data. Overall, Table IV supports that the bias-correction enhances the overall reliability of the climate models, demonstrating a robust alignment with the observed data, as also corroborated by the results shown in Fig. 5.

In Fig. 5, the observed data are set as the reference point (denoted by the red square). The proximity of the NBC and BC points to this reference indicates the degree of agreement in SD, centered RMSE, and R with the observed data. The bold red arc in each diagram marks the trajectory of the bias-corrected outputs, demonstrating their alignment with observed data in terms of SD. This alignment indicates that the bias-correction method successfully adjusts the GCMs to better reflect the observed variability of each parameter. For three weather parameters (i.e., DBT, EWS, and NWS), the Taylor diagrams show that the bias-correction maintains or decreases the centered RMSE. With the exception of GHI, RH, AP, and TSC where a slight increase in RMSE is observed, suggesting a marginal loss in accuracy post-correction for these specific parameters. Meanwhile, the R value remains almost unchanged by the bias-correction process, indicating that the linear relationship with observed data are maintained.

D. A case study for building energy consumption

At the fourth quarter of 2023, about 29% (2.18×10^6 people) of the population were living in 856 700 public rental houses (PRH) of the Housing Authority and Hong Kong Housing Society according to the Hong Kong SAR Government yearbook 2023 (https://www.yearbook.gov.hk/2023/en/pdf/E08.pdf). Most of the PRH are high-rise buildings that consist of about 40 stories. To understand future energy demand during changing climate conditions, this study considers three common PRH layouts. The Trident-type building, which is a Y-

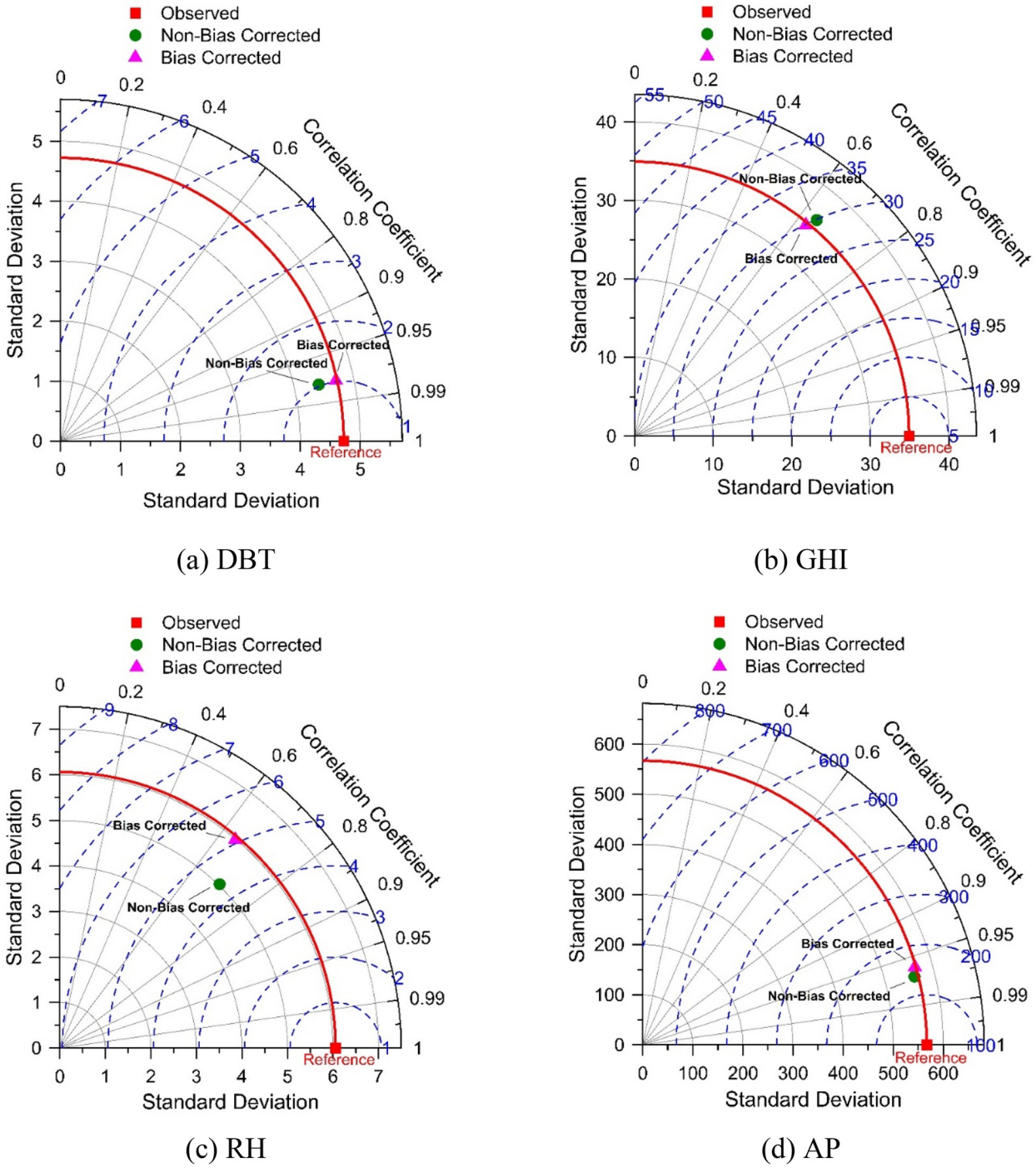

FIG. 5. Taylor diagrams for weather parameters.

shaped building layout [Fig. 6(a)], is a common PRH type built in the 1980s. The slab type building, with a Z-shaped building layout [Fig. 6(b)], is another common building type in PRH schemes. Harmony, a popular PRH in Hong Kong, consists of a cruciform building layout [Fig. 6(c)]. A typical floor of three PRH buildings was first modeled in Autodesk Revit software with the physical and thermal properties described in Table V. The remaining floors were modeled as adiabatic walls to minimize the computation time.

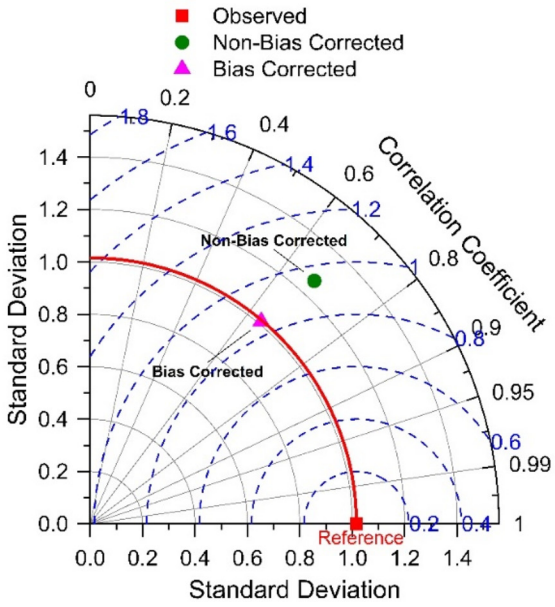

(e) EWS

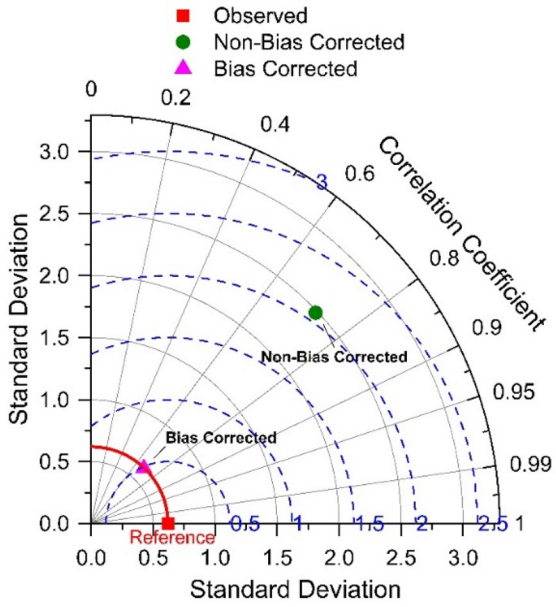

(f) NWS

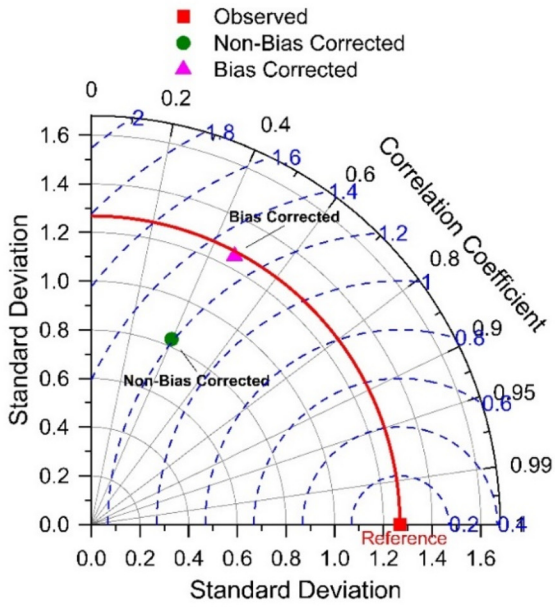

(g) TSC

FIG. 5. (*Continued.*)

Table VI presents the heat-gain information, cooling and heating set points, and occupancy schedules set in space properties of the BIM model. Only the bedrooms and living rooms of PRH are equipped with Heating, Ventilation, and Air Conditioning (HVAC) systems, and those spaces were defined as conditioned spaced in the BIM model. The BIM model was then converted into EnergyPlus input format, IDF file using a tool developed by Perera *et al.*[58] In the IDF file, HVAC systems were assigned as unitary systems, with a cooling coil

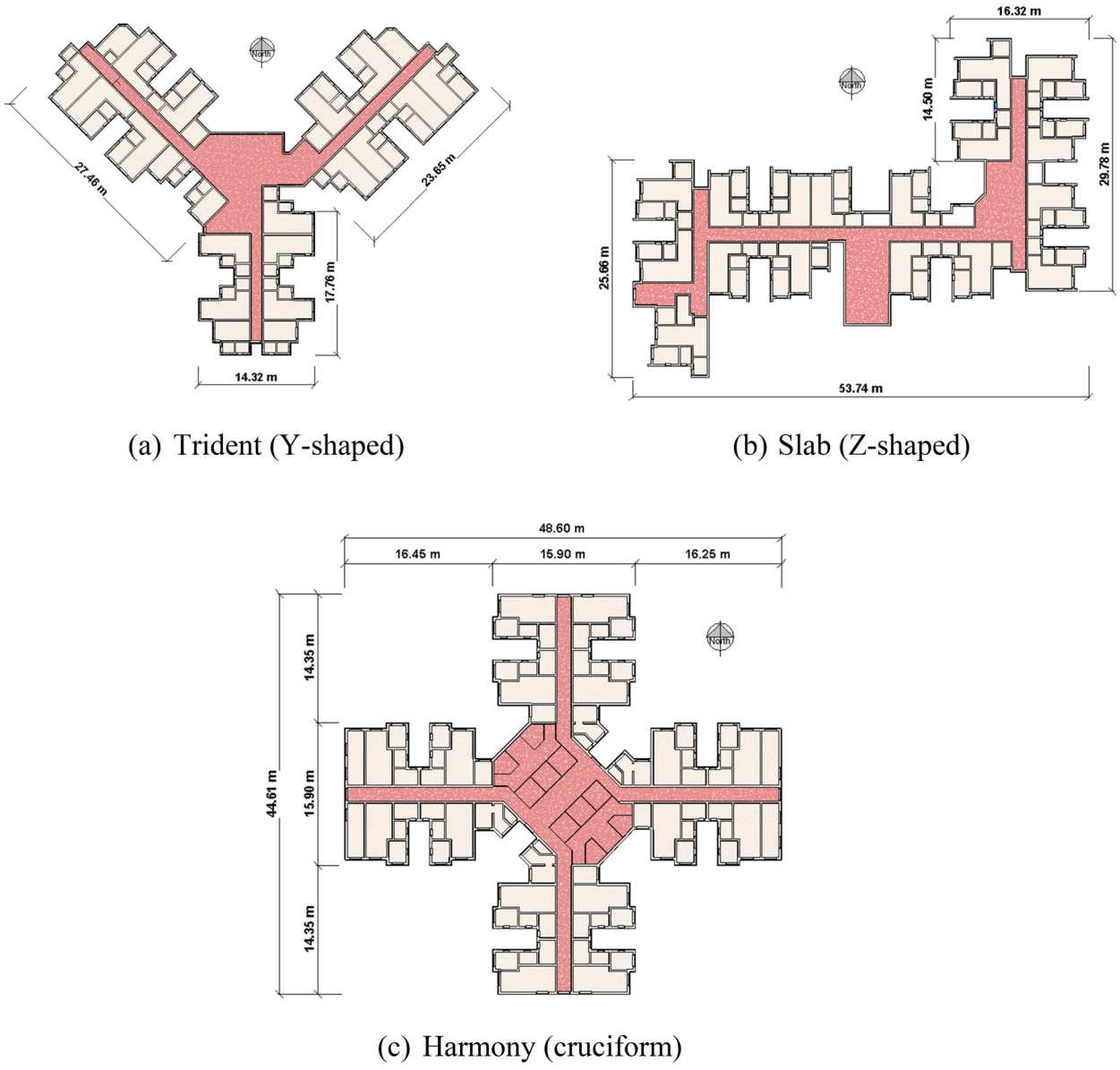

FIG. 6. Plane view of three typical shapes of PRH in Hong Kong.

coefficient of performance (COP) of 3.0. The HVAC systems were programed to activate during occupancy periods if the indoor temperature, exceeds 26 °C (cooling setpoint) or drops below 20 °C (heating setpoint) as specified in Table VI. Outside these conditions, it is assumed that occupants will open windows, allowing for natural ventilation, which is modeled with an air change rate of 3 air changes per hour (3 ach). Using three IDF files prepared for three PRH buildings, a total of 37 EnergyPlus simulations were performed using 13 weather files (historical weather file and near future, mid future, and far future timeframes under 4 SSP scenarios) prepared according to Sec. II E. Subsequently, the EUI [Eq. (1)] of each scenario was obtained from the simulation to evaluate the climate change impacts on PRH energy consumption.

Figure 7 demonstrates the energy consumption trends for three types of PRH buildings—Harmony, Trident, and Slab—under different SSP climate scenarios. Each graph contains four different SSPs (SSP1-2.6, SSP2-4.5, SSP3-7.0, and SSP5-8.5), projecting the building operational energy consumption from historical to far-future scenarios. The analysis reveals that the Trident type PRH consistently exhibits the highest energy consumption, followed by the Harmony type, and the Slab type PRH has the lowest energy consumption for all scenarios and periods. Under historical climate conditions, the Trident

TABLE V. Physical properties of the target PRH buildings.

Configuration/thermal properties of elements	Harmony	Trident	Slab
Number of stories		40	
Floor height (m)	2.7	2.7	2.6
Floor area (m^2)	952.5	779.5	809.3
Conditioned area (heating and cooling) (m^2)	517.3	470	458.8
External wall			
Mosaic tile (mm)		5	
Polystyrene insulation (mm)		50	
Reinforced concrete (mm)	235	135	175
Gypsum plaster(mm)		13	
Internal wall			
Gypsum plaster (mm)		15	
Concrete (mm)		170	
Gypsum plaster (mm)		15	
Exterior glazing			
U value ($W/m^2 K$)		5.75	
SHGC		0.77	

type consumes 6.3 kWh/m^2 more energy than the Slab type and 4.0 kWh/m^2 more than the Harmony type. This difference remains visible across all future climate scenarios, indicating a persistent variation in energy demand based on building design.

Across the SSPs, there is a clear upward trend in EUI for all building types over the next 75 years in Fig. 7, reflecting the growing energy demands driven by the changing climate. The mildest energy consumption pathway is observed in the SSP1-2.6, where energy consumption increases are the lowest, the increase in EUI for Harmony, Trident, and Slab buildings will be relatively moderate, with increases of 4.5%, 4.2%, and 4.0%, respectively. In contrast, the SSP5-8.5 scenario shows the most significant rise in EUI, with an increase in approximately 14.0%, 12.8%, and 12.4% by the end of the century for Harmony, Trident, and Slab PRH, respectively. The results highlight the significant impact of climate change on building energy demand, with extreme scenarios resulting in considerably higher energy requirements and emphasize the need for targeted interventions in building design and energy efficiency strategies, especially for more energy-intensive PRH like the Harmony type, to mitigate the effects of future climate scenarios.

TABLE VI. Heat gain and schedules for the target PRH buildings.

Parameter	Value
Occupant density (m^2/people)	12
Occupant load (W/person)	110
Lighting power density (W/m^2)	17
Equipment power density (W/m^2)	12
Heating setpoint (°C)	20
Cooling setpoint (°C)	26
Occupancy schedule	Bedroom – All days 13:00–07:00 Livingroom/other rooms – All days 13:00–22:00

Figure 7 also reveals trends in the steepness of the curves for each SSP scenario, reflecting the rate of increase in energy consumption over time. Under the SSP1-2.6 scenario, the EUI for all three PRH building types shows moderate growth from the historical period through the near and mid-century future. However, the rate of growth begins to decelerate in the far future, suggesting a stabilization in energy demand as the climate scenario projects more restrained temperature increases. This suggests that SSP1-2.6, the most optimistic scenario, offers a pathway to limiting the long-term rise in energy consumption, potentially due to a combination of climate mitigation efforts and less extreme warming. In contrast, the SSP2-4.5 and SSP3-7.0 scenarios show relatively slow increases in EUI from the historical period to the near future. However, the rate of increase becomes steeper as the time move from the near to the far future, indicating an acceleration in energy demand growth as the climate warms more significantly in these scenarios. This sharp rise in energy consumption in the mid-century to far future reflects the higher global temperatures and more significant climate impacts projected under SSP2-4.5 and SSP3-7.0. As temperatures continue to rise, buildings may require more energy for cooling to maintain comfort levels, driving the steeper increase in EUI. For the most extreme climate scenario—SSP5-8.5, energy consumption grows at a relatively modest rate during the near future. However, from then onward through the mid-century to the far future, the rate of growth increases sharply, resulting in a rapid rise in EUI which corresponds with the dramatic increase in global temperatures projected under SSP5-8.5. The significant rise in energy consumption in this scenario highlights the severe energy challenges that may emerge if aggressive climate action is not taken.

Figure 7(a) depicts EUI across various SSPs shows an intriguing trend in the near future, where SSP5-8.5 records the lowest EUI, while SSP1-2.6 displays moderate results, deviating from their positions in other periods. The lower EUI under SSP5-8.5 in the near future is an interesting point, particularly as this pathway typically implies a trajectory with higher energy demand due to rapid industrialization and less stringent policies on emissions. Conversely, SSP1-2.6 displaying moderate results in the near future, instead of its typically lower EUI, could indicate that the early implementation of stringent sustainability measures and technologies has not yet achieved full effectiveness or that these measures initially require higher energy inputs before they lead to lower energy use as efficiencies improve and renewable technologies become more widespread and effective. The crossing of lines between SSP2-4.5 and SSP3-7.0 in the mid-future suggests a transitional phase where the energy consumption trajectories under these two scenarios converge and then diverge. This cross could indicate a point at which the underlying factors of these scenarios—such as economic growth, energy policies, or technological advancements—temporarily align before diverging due to differing long-term strategies or implementations. Similar conclusions can be obtained from Figs. 7(b) and 7(c).

IV. CONCLUDING REMARKS

This study contributes to the understanding of climate change impacts at a regional level (i.e., Hong Kong) by utilizing GCMs projections derived from the CMIP6. Incorporating 44 GCMs under four representative emission scenarios (i.e., SSP1-2.6, SSP2-4.5, SSP3-7.0,

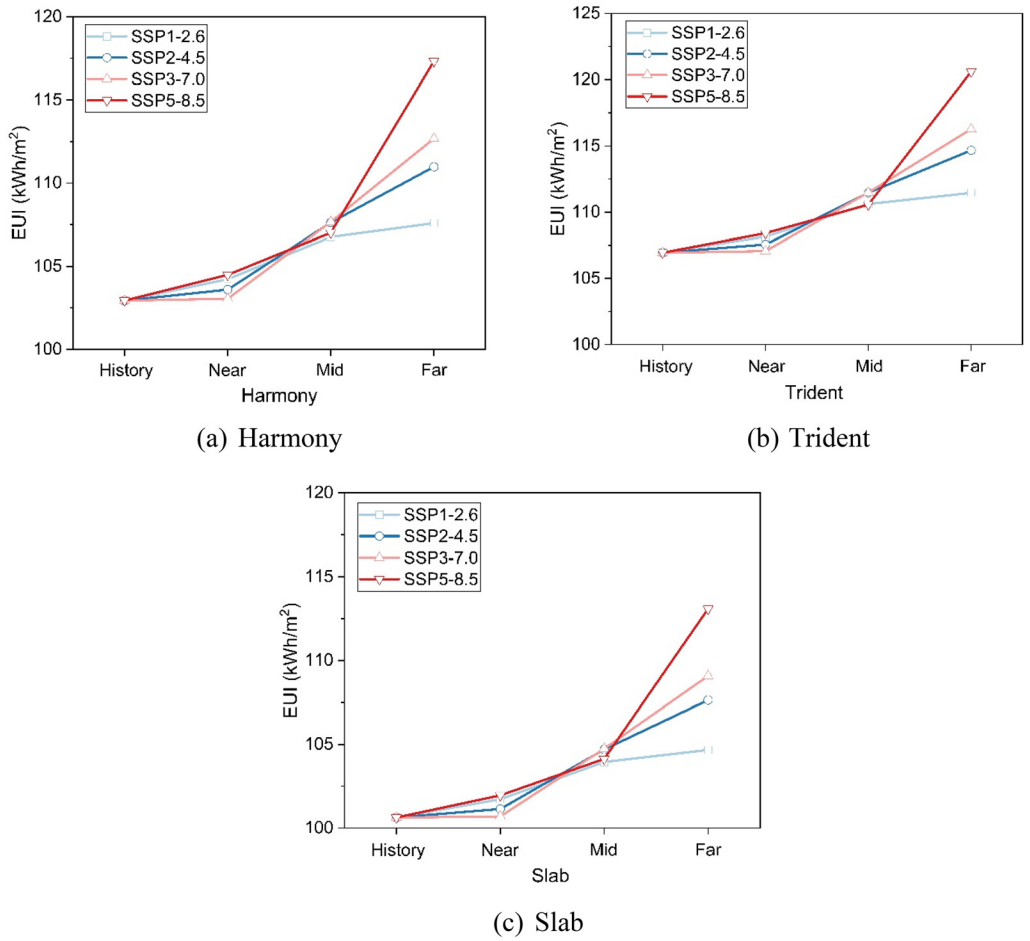

(a) Harmony (b) Trident

(c) Slab

FIG. 7. Energy consumption of three typical PRH buildings under SSP1-2.6, SSP2-4.5, SSP3-7.0, and SSP5-8.5, where "History" means historical scenario from 1981 to 2014, "Near" means near future from 2015 to 2044, "Mid" means mid-century future from 2045 to 2074, and "Far" means far future from 2075 to 2100.

SSP5-8.5), the research demonstrates a robust method for enhancing the utility of GCM outputs through the application of bilinear interpolation and morphing statistical downscaling methods and a dual bias-correction technique. The validation uses meteorological observation data from the Hong Kong Observatory King's Park station that confirms their effectiveness. The comprehensive future weather data obtaining framework proposed in this study not only minimized the biases inherent in the original GCM outputs but also achieved a higher temporal and spatial resolution climatology data. This resolution enhancement is important for accurate assessing the climate impacts on building energy consumptions.

The projected weather data are applied in EnergyPlus simulations to forecast future energy consumption patterns in PRH buildings in Hong Kong. The analysis reveals differences in operational EUI across the three building types—Trident, Harmony, and Slab—under different SSP scenarios. For example, under current conditions, the Trident type consumes 6.3 kWh/m^2 more energy than the Slab type, and 4.0 kWh/m^2 more than the Harmony type. The variations continue across future scenarios, with the most significant increases in the SSP5-8.5, where the Harmony, Trident, and Slab types of experience EUI increases of 14.0%, 12.8%, and 12.4%, respectively, by the end of the century. In contrast, under the slight climate change scenario—SSP1-2.6, energy demand increases more modestly, with projected EUI rises of 4.5%, 4.2%, and 4.0%, respectively. The analysis for the rate of energy consumption growth across SSP scenarios reveals that under SSP1-2.6, growth is moderate and stabilizes in the far future, suggesting that this scenario offers a pathway to controlling energy demand. In more extreme scenarios, such as SSP2-4.5 and SSP3-7.0, the rate of growth accelerates significantly toward the far future, driven by rising global temperatures. SSP5-8.5 shows a sharp rise in energy demand in the far future, emphasizing the urgent need for climate action. These findings highlight the significant impact of climate change on building energy demand and the need for adaptive design strategies and energy efficiency improvements, particularly for energy-intensive buildings, such as the Harmony type.

This study is limited by its focus on PRH buildings in Hong Kong, which may not reflect energy consumption trends in other building types or locations. Future research should consider a wider range of buildings and regions. Additionally, while the bias-correction improve the accuracy of climate projections and downscaling results,

TABLE VII. List of CMIP6 general circulation models (GCMs) applied in this study.

source_id	institution_id	Institution	Country	release_ year	resolution (lat × lon)	nominal_ resolution
ACCESS-CM2	CSIRO	Commonwealth Scientific and Industrial Research Organization (CSIRO)	Australia	2019	144 × 192	250 km
AWI-CM-1-1-MR	AWI	Alfred Wegener Institute	Germany	2018	192 × 384	100 km
BCC-CSM2-MR	BCC	Beijing Climate Center	China	2017	160 × 320	100 km
CAMS-CSM1-0	CAMS	Chinese Academy of Meteorological Sciences	China	2016	160 × 320	100 km
CanESM5	CCCma	Canadian Center for Climate Modeling and Analysis	Canada	2019	64 × 128	500 km
CAS-ESM2-0	CAS	Chinese Academy of Sciences	China	2019	128 × 256	100 km
CESM2	NCAR	National Center for Atmospheric Research (NCAR)	USA	2018	192 × 288	100 km
CESM2-FV2	NCAR	National Center for Atmospheric Research (NCAR)	USA	2019	96 × 144	250 km
CESM2-WACCM	NCAR	National Center for Atmospheric Research (NCAR)	USA	2018	192 × 288	100 km
CESM2-WACCM-FV2	NCAR	National Center for Atmospheric Research (NCAR)	USA	2018	96 × 144	250 km
CIESM	THU	Department of Earth System Science	China	2017	192 × 288	100 km
CMCC-CM2-HR4	CMCC	Fondazione Centro Euro-Mediterraneo sui Cambiamenti Climatici	Italy	2016	192 × 288	100 km
CMCC-CM2-SR5	CMCC	Fondazione Centro Euro-Mediterraneo sui Cambiamenti Climatici	Italy	2016	192 × 288	100 km
CMCC-ESM2	CMCC	Fondazione Centro Euro-Mediterraneo sui Cambiamenti Climatici	Italy	2017	192 × 288	100 km
CNRM-CM6-1	CNRM-CERFACS	Center National de Recherches Meteorologiques (CNRM)	France	2017	···	250 km
CNRM-CM6-1-HR	CNRM-CERFACS	Center National de Recherches Meteorologiques (CNRM)	France	2017	···	100 km
CNRM-ESM2-1	CNRM-CERFACS	Center National de Recherches Meteorologiques (CNRM)	France	2017	···	250 km
E3SM-1-0	E3SM-Project	Lawrence Livermore National Laboratory (LLNL)	USA	2018	90 × 90	100 km
E3SM-1-1	E3SM-Project	Lawrence Livermore National Laboratory (LLNL)	USA	2019	90 × 90	100 km
E3SM-1-1-ECA	E3SM-Project	Lawrence Livermore National Laboratory (LLNL)	USA	2019	90 × 90	100 km
E3SM-2-0	E3SM-Project	Lawrence Livermore National Laboratory (LLNL)	USA	2022	···	100 km
E3SM-2-0-NARRM	E3SM-Project	Lawrence Livermore National Laboratory (LLNL)	USA	2022	···	100 km
EC-Earth3	EC-Earth-Consortium	EC-Earth consortium	Sweden	2019	256 × 512	100 km
EC-Earth3-AerChem	EC-Earth-Consortium	EC-Earth consortium	Sweden	2019	256 × 512	100 km
EC-Earth3-CC	EC-Earth-Consortium	EC-Earth consortium	Sweden	2019	256 × 512	100 km
EC-Earth3-Veg	EC-Earth-Consortium	EC-Earth consortium	Sweden	2019	256 × 512	100 km
EC-Earth3-Veg-LR	EC-Earth-Consortium	EC-Earth consortium	Sweden	2019	160 × 320	250 km
FGOALS-f3-L	CAS	Chinese Academy of Sciences	China	2017	180 × 360	100 km

TABLE VII. (*Continued.*)

source_id	institution_id	Institution	Country	release_ year	resolution (lat × lon)	nominal_ resolution
FGOALS-g3	CAS	Chinese Academy of Sciences	China	2017	80 × 180	250 km
FIO-ESM-2-0	FIO-QLNM	First Institute of Oceanography (FIO)	China	2018	192 × 288	100 km
GFDL-ESM4	NOAA-GFDL	National Oceanic and Atmospheric Administration	USA	2018	180 × 360	100 km
HadGEM3-GC31-MM	MOHC	Met Office Hadley Center	UK	2016	324 × 432	100 km
INM-CM4-8	INM	Institute for Numerical Mathematics (INM)	Russia	2016	120 × 180	100 km
INM-CM5-0	INM	Institute for Numerical Mathematics (INM)	Russia	2016	120 × 180	100 km
IPSL-CM6A-LR	IPSL	Institut Pierre Simon Laplace (IPSL)	France	2017	143 × 144	250 km
KIOST-ESM	KIOST	Korea Institute of Ocean Science and Technology (KIOST)	Republic of Korea	2018	96 × 192	250 km
MIROC6	MIROC	Japan Agency for Marine-Earth Science and Technology (JAMSTEC)	Japan	2017	128 × 256	250 km
MPI-ESM1-2-HR	MPI-M DWD DKRZ	Max Planck Institute for Meteorology (MPI-M)	Germany	2017	192 × 384	100 km
MPI-ESM1-2-LR	MPI-M DWD DKRZ	Max Planck Institute for Meteorology (MPI-M)	Germany	2017	96 × 192	250 km
MRI-ESM2-0	MRI	Meteorological Research Institute (MRI)	Japan	2017	160 × 320	100 km
NESM3	NUIST	Nanjing University of Information Science and Technology (NUIST)	China	2016	96 × 192	250 km
NorESM2-MM	NCC	NorESM Climate modeling Consortium	Norway	2017	192 × 288	100 km
SAM0-UNICON	SNU	Seoul National University (SNU)	Republic of Korea	2017	192 × 288	100 km
TaiESM1	AS-RCEC	Research Center for Environmental Changes	Taiwan	2018	192 × 288	100 km

the correction processes are based on constant error/trend assumption compared with the historical data, and it may not account for unexpected climate changes. Furthermore, in the future work, the scope of the study should be expanded to include comparisons with other regional or global climate change studies. While this study focuses on the overall impact of climate change on building EUI, the relative contributions of individual weather variables to the climate change signal are not quantified, and this could be an important area for future research. Finally, this study assumes static building operation, and future research should incorporate dynamic scenarios to account for evolving technology, occupant behavior, and policy changes that may influence future energy demand.

ACKNOWLEDGMENTS

This work was supported by the grants from Guangdong Basic and Applied Basic Research Foundation (Project No. 2022B1515130006). The authors acknowledge the support from the Tsinghua Shenzhen International Graduate School—Shenzhen Pengrui Young Faculty Program of Shenzhen Pengrui Foundation (No. SZPR2023003).

AUTHOR DECLARATIONS

Conflict of Interest

The authors have no conflicts to disclose.

Author Contributions

Jiayao Wang: Data curation (equal); Visualization (equal); Writing – original draft (equal); Writing – review & editing (equal). **Binura J. Kudagama:** Data curation (equal); Methodology (equal); Validation (equal); Writing – original draft (equal). **Udara S. Perera:** Data curation (equal); Visualization (equal); Writing – review & editing (equal). **Sunwei Li:** Funding acquisition (equal); Supervision (equal). **Xuelin Zhang:** Writing – review & editing (equal).

DATA AVAILABILITY

The data that support the findings of this study are available from the corresponding authors upon reasonable request.

TABLE VIII. List of CMIP6 GCMs collected under each climate variable and their experiments (historical and future SSP scenarios).

	Tas					tasmax					tasmin					hurs				
	Historical	SSPl-2.6	SSP2-4.5	SSP3-7.0	SSP5-8.5	Historical	SSP1-2.6	SSP2-4.5	SSP3-7.0	SSP5-8.5	Historical	SSPl-2.6	SSP2-4.5	SSP3-7.0	SSP5-8.5	Historical	SSPl-2.6	SSP2-4.5	SSP3-7.0	SSP5-8.5
ACCESS-CM2							X	X	X	X		X	X	X	X					
AWI-CM-1-1-MR	X	X	X	X	X	X	X	X	X	X	X	X	X	X	X	X	X	X	X	X
BCC-CSM2-MR	X	X	X	X	X	X	X	X	X	X	X	X	X	X	X	X	X	X	X	X
CAMS-CSMl-0	X	X	X	X	X												X	X	X	X
CanESM5																				
CAS-ESM2-0	X	X	X	X	X												X	X	X	X
CESM2	X	X	X	X	X		X	X	X	X		X	X	X	X					
CESM2-FV2	X			X	X															
CESM2-WACCM	X	X	X	X	X			X					X							
CESM2-WACCM-FV2	X																			
CIESM	X	X	X		X															
CMCC-CM2-HR4	X															X				
CMCC-CM2-SR5	X	X	X	X	X	X					X					X	X	X	X	X
CMCC-ESM2	X	X	X	X	X	X	X	X		X	X	X	X		X	X	X	X	X	X
CNRM-CM6-1							X	X	X	X		X	X	X	X					
CNRM-CM6-l-HR							X			X		X			X					
CNRM-ESM2-1							X	X	X	X		X	X	X	X					
E3SM-1-0	X					X					X					X				X
E3SM-1-1	X				X															
E3SM-1-1-ECA	X				X															
E3SM-2-0	X																			
E3SM-2-0-NARRM	X																			
EC-Earth3	X	X	X	X	X															
EC-Earth3-AerChem	X			X	X	X			X		X			X		X			X	
EC-Earth3-CC	X		X			X		X		X	X		X		X	X		X		X
EC-Earth3-Veg	X	X																		
EC-Earth3-Veg-LR		X	X	X	X		X	X	X	X			X	X	X		X	X	X	X
FGOALS-f3-L	X	X	X	X	X	X					X						X	X	X	X
FGOALS-g3							X		X			X		X						
FIO-ESM-2-0	X	X	X		X											X	X	X		X
GFDL-ESM4	X	X	X	X	X	X	X	X	X	X	X	X			X	X	X	X	X	X
HadGEM3-GC31-MM	X	X			X											X	X			X
INM-CM4-8	X	X	X	X	X	X	X	X	X	X	X	X	X	X	X	X	X	X	X	X
INM-CM5-0	X	X	X	X	X	X	X	X	X	X	X	X	X	X	X	X	X	X	X	X
IPSL-CM6A-LR								X				X	X	X	X					
KIOST-ESM							X	X		X										
MIROC6							X	X	X	X		X	X	X	X					
MPI-ESMl-2-HR	X	X	X	X	X	X					X					X	X	X	X	X
MPI-ESMl-2-LR							X	X	X	X		X	X	X	X					

TABLE VIII. (*Continued.*)

	Tas					tasmax					tasmin					hurs				
	Historical	SSPl-2.6	SSP2-4.5	SSP3-7.0	SSP5-8.5	Historical	SSP1-2.6	SSP2-4.5	SSP3-7.0	SSP5-8.5	Historical	SSPl-2.6	SSP2-4.5	SSP3-7.0	SSP5-8.5	Historical	SSPl-2.6	SSP2-4.5	SSP3-7.0	SSP5-8.5
MRI-ESM2-0	X	X	X	X	X	X	X	X	X	X	X	X	X	X	X		X	X	X	X
NESM3								X		X			X		X					
NorESM2-MM	X	X	X	X	X	X	X	X	X	X	X	X	X	X	X		X	X	X	X
SAMO-UNICON	X					X					X									
TaiESMl	X	X	X	X	X	X					X					X	X	X	X	X
Count	32	22	21	20	25	16	18	20	16	19	16	17	18	16	19	15	17	17	16	19

psl					rsds					uas					vas					clt					
Historical	SSP1-2.6	SSP2-4.5	SSP3-7.0	SSP5-8.5	Historical	SSP1-2.6	SSP2-4.5	SSP3-7.0	SSP5-8.5	Historical	SSP1-2.6	SSP2-4.5	SSP3-7.0	SSP5-8.5	Historical	SSP1-2.6	SSP2-4.5	SSP3-7.0	SSP5-8.5	Historical	SSP1-2.6	SSP2-4.5	SSP3-7.0	SSP5-8.5	Count
																									8
X	X	X	X	X	X	X	X	X	X	X	X	X	X	X	X	X	X	X	X	X	X	X	X	X	45
X	X	X	X	X	X	X	X	X	X	X	X	X	X	X	X	X	X	X	X	X	X	X	X	X	45
X	X	X	X	X	X	X	X	X	X	X	X	X	X	X	X	X	X	X	X	X	X	X	X	X	34
											X	X	X	X	X	X	X	X	X						9
X	X	X	X	X	X	X	X	X	X	X	X	X	X	X	X	X	X	X	X	X	X	X	X	X	34
X	X	X	X	X	X	X	X	X	X											X	X	X	X	X	28
X					X															X					6
X			X	X	X	X	X	X	X											X			X		17
X					X															X					4
X	X	X		X	X	X	X		X	X											X	X		X	16
X					X					X					X					X					7
X	X	X	X	X	X	X	X	X	X	X	X	X	X	X	X	X	X	X	X	X	X	X	X	X	37
X	X	X	X	X	X	X	X	X	X	X	X	X	X	X	X	X	X	X	X	X	X	X	X	X	43
																									8
																									4
																									8
X					X															X				X	9
X				X	X				X											X				X	8
X					X															X					5
																									1
																									1
																									5
X			X		X			X		X			X		X					X					17
X		X		X	X		X		X	X		X		X	X		X	X	X	X		X		X	27
																									2
	X	X	X	X		X	X	X	X		X	X	X	X		X	X	X	X	X	X	X	X	X	36
X	X	X	X	X	X	X	X	X	X	X	X	X	X	X	X	X	X	X	X	X	X	X	X	X	36
																									4

TABLE VIII. (*Continued*.)

psl					rsds					uas					vas					clt				
Historical	SSP1-2.6	SSP2-4.5	SSP3-7.0	SSP5-8.5	Historical	SSP1-2.6	SSP2-4.5	SSP3-7.0	SSP5-8.5	Historical	SSP1-2.6	SSP2-4.5	SSP3-7.0	SSP5-8.5	Historical	SSP1-2.6	SSP2-4.5	SSP3-7.0	SSP5-8.5	Historical	SSP1-2.6	SSP2-4.5	SSP3-7.0	SSP5-8.5	Count
X		X	X		X		X	X	X			X	X	X			X	X	X	X		X	X	X	20
X		X	X	X	X		X	X	X			X	X	X			X	X	X	X		X	X	X	43
X		X	X		X		X	X	X			X	X	X			X	X	X			X	X	X	21
X		X	X	X	X		X	X	X			X	X	X			X	X	X	X		X	X	X	44
X		X	X	X	X		X	X	X			X	X	X			X	X	X	X		X	X	X	45
																									5
																									3
																									8
X		X	X		X		X	X	X			X	X	X			X	X	X	X		X	X	X	37
																									8
X		X	X		X		X	X	X			X	X	X			X	X	X	X		X	X	X	44
																									4
X		X	X		X		X	X	X			X	X	X			X	X	X	X		X	X	X	34
X					X																				6
X		X	X		X		X	X	X			X	X	X			X	X	X	X		X	X	X	27
28		19	19	18	20		20	18	22	17	15	15	15	15	17	15	15	15	16	28	19	19	17	22	853

APPENDIX: LIST OF CMIP6 GENERAL CIRCULATION MODELS

List of CMIP6 general circulation models (GCMs) applied in this study. List of CMIP6 GCMs collected under each climate variable and their experiments (historical and future SSP scenarios).

REFERENCES

[1]A. Chan, "Developing future hourly weather files for studying the impact of climate change on building energy performance in Hong Kong," Energy Build. **43**, 2860–2868 (2011).

[2]IPCC, "Climate change 2021: The physical science basis," in *Contribution of Working Group I to the Sixth Assessment Report of the Intergovernmental Panel on Climate Change* (Cambridge University Press, 2021).

[3]IPCC, "Climate change 2022: Impacts, adaptation and vulnerability," in *IPCC Sixth Assessment Report. Contribution of Working Group II to the Sixth Assessment Report of the Intergovernmental Panel on Climate Change*, edited by H.-O. Pörtner, D. C. Roberts, H. Adams, C. Adler, P. Aldunce, E. Ali *et al.* (Cambridge University Press, Cambridge, UK and New York, NY, 2022), p. 3056.

[4]IPCC, "Climate change 2023: Synthesis report, summary for policymakers," in *Contribution of Working Groups I, II and III to the Sixth Assessment Report of the Intergovernmental Panel on Climate Change*, edited by Core Writing Team, H. Lee, and J. Romero (IPCC, Geneva, Switzerland, 2023).

[5]S. Liu, Y. T. Kwok, K. K.-L. Lau, H. W. Tong, P. W. Chan, and N. Edward, "Development and application of future design weather data for evaluating the building thermal-energy performance in subtropical Hong Kong," Energy Build. **209**, 109696 (2020).

[6]Y. Liu, D. Chen, S. Li, and P. Chan, "Discerning the spatial variations in offshore wind resources along the coast of China via dynamic downscaling," Energy **160**, 582–596 (2018).

[7]F. Feser, B. Rockel, H. von Storch, J. Winterfeldt, and M. Zahn, "Regional climate models add value to global model data: A review and selected examples," Bull. Am. Meteorol. Soc. **92**, 1181–1192 (2011).

[8]R. Laprise, "Regional climate modelling," J. Comput. Phys. **227**, 3641–3666 (2008).

[9]M. Ekström, M. R. Grose, and P. H. Whetton, "An appraisal of downscaling methods used in climate change research," Wiley Interdiscip. Rev. Clim. Change **6**, 301–319 (2015).

[10]E. Rodrigues, M. S. Fernandes, and D. Carvalho, "Future weather generator for building performance research: An open-source morphing tool and an application," Build. Environ. **233**, 110104 (2023).

[11]S. E. Belcher, J. N. Hacker, and D. S. Powell, "Constructing design weather data for future climates," Build. Serv. Eng. Res. Technol. **26**, 49–61 (2005).

[12]X. Li, Z. Li, W. Huang, and P. Zhou, "Performance of statistical and machine learning ensembles for daily temperature downscaling," Theor. Appl. Climatol. **140**, 571–588 (2020).

[13]J. Fiddes, K. Aalstad, and M. Lehning, "TopoCLIM: Rapid topography-based downscaling of regional climate model output in complex terrain v1. 1," Geosci. Model Dev. **15**, 1753–1768 (2022).

[14]L. M. King, A. I. McLeod, and S. P. Simonovic, "Improved weather generator algorithm for multisite simulation of precipitation and temperature," J. Am. Water Resour. Assoc. **51**, 1305–1320 (2015).

[15]Z. Zeng, J. H. Kim, H. Tan, Y. Hu, P. Rastogi, J. Wang *et al.*, "A critical analysis of future weather data for building and energy modeling," in Proceedings of the Building Simulation, 2023.

[16]H. Wang and Q. Chen, "Impact of climate change heating and cooling energy use in buildings in the United States," Energy Build. **82**, 428–436 (2014).

[17]T. Shibuya and B. Croxford, "The effect of climate change on office building energy consumption in Japan," Energy Build. **117**, 149–159 (2016).

[18]P. Shen and N. Lior, "Vulnerability to climate change impacts of present renewable energy systems designed for achieving net-zero energy buildings," Energy **114**, 1288–1305 (2016).

[19]M. F. Jentsch, P. A. James, L. Bourikas, and A. S. Bahaj, "Transforming existing weather data for worldwide locations to enable energy and building

performance simulation under future climates," Renewable Energy **55**, 514–524 (2013).
[20]P. Shen, "Impacts of climate change on US building energy use by using downscaled hourly future weather data," Energy Build. **134**, 61–70 (2017).
[21]R.-L. Hwang, W.-M. Shih, T.-P. Lin, and K.-T. Huang, "Simplification and adjustment of the energy consumption indices of office building envelopes in response to climate change," Appl. Energy **230**, 460–470 (2018).
[22]M. Cellura, F. Guarino, S. Longo, and G. Tumminia, "Climate change and the building sector: Modelling and energy implications to an office building in southern Europe," Energy Sustainable Dev. **45**, 46–65 (2018).
[23]Z. J. Zhai and J. M. Helman, "Implications of climate changes to building energy and design," Sustainable Cities Soc. **44**, 511–519 (2019).
[24]J. Chai, P. Huang, and Y. Sun, "Investigations of climate change impacts on net-zero energy building lifecycle performance in typical Chinese climate regions," Energy **185**, 176–189 (2019).
[25]J. Wang, K. T. Tse, S. Li, and J. C. Fung, "Prediction of the typhoon wind field in Hong Kong: Integrating the effects of climate change using the Shared Socioeconomic Pathways," Clim. Dyn. **59**, 2311–2329 (2022).
[26]J. Wang, S. Cao, R. Zhang, S. Li, and T. K. Tse, "Uncertainty of typhoon extreme wind speeds in Hong Kong integrating the effects of climate change," Phys. Fluids **36**, 087126 (2024).
[27]J. Wang, K. T. Tse, and S. W. Li, "Integrating the effects of climate change using representative concentration pathways into typhoon wind field in Hong Kong," in 8th European African Conference on Wind Engineering, Bucharest, Romania, 2022.
[28]B. C. O'Neill, C. Tebaldi, D. P. Van Vuuren, V. Eyring, P. Friedlingstein, G. Hurtt *et al.*, "The scenario model intercomparison project (ScenarioMIP) for CMIP6," Geosci. Model Dev. **9**, 3461–3482 (2016).
[29]V. Eyring, S. Bony, G. A. Meehl, C. A. Senior, B. Stevens, R. J. Stouffer *et al.*, "Overview of the Coupled Model Intercomparison Project Phase 6 (CMIP6) experimental design and organization," Geosci. Model Dev. **9**, 1937–1958 (2016).
[30]H. Kikumoto, R. Ooka, Y. Arima, and T. Yamanaka, "Study on the future weather data considering the global and local climate change for building energy simulation," Sustainable Cities Soc. **14**, 404–413 (2015).
[31]M. Hosseini, A. Bigtashi, and B. Lee, "Generating future weather files under climate change scenarios to support building energy simulation—A machine learning approach," Energy Build. **230**, 110543 (2021).
[32]S. Li, Z. Z. Hu, K. T. Tse, and A. Weerasuriya, "Wind direction field under the influence of topography: Part II: CFD investigations," Wind Struct. **22**, 477–501 (2016).
[33]E. Hawkins and R. Sutton, "The potential to narrow uncertainty in regional climate predictions," Bull. Am. Meteorol. Soc. **90**, 1095–1108 (2009).
[34]D. B. Crawley, J. W. Hand, and L. K. Lawrie, "Improving the weather information available to simulation programs," in *Proceedings of Building Simulation'99* (IBPSA, 1999), pp. 529–536.
[35]H. Li, Y. Yang, K. Lv, J. Liu, and L. Yang, "Compare several methods of select typical meteorological year for building energy simulation in China," Energy **209**, 118465 (2020).
[36]J. C. Lam, K. K. Wan, S. Wong, and T. N. Lam, "Principal component analysis and long-term building energy simulation correlation," Energy Convers. Manage. **51**, 135–139 (2010).
[37]M. Kamruzzaman, S. Wahid, S. Shahid, E. Alam, M. Mainuddin, H. T. Islam *et al.*, "Predicted changes in future precipitation and air temperature across Bangladesh using CMIP6 GCMs," Heliyon **9**, e16274 (2023).
[38]J. Wang, K. T. Tse, S. Li, and C. H. Fung, "A model of the sea–land transition of the mean wind profile in the tropical cyclone boundary layer considering climate changes," Int. J. Disaster Risk Sci. **14**, 413 (2023).
[39]Y. Yue, D. Yan, Q. Yue, G. Ji, and Z. Wang, "Future changes in precipitation and temperature over the Yangtze River Basin in China based on CMIP6 GCMs," Atmos. Res. **264**, 105828 (2021).
[40]D. M. Jose, A. M. Vincent, and G. S. Dwarakish, "Improving multiple model ensemble predictions of daily precipitation and temperature through machine learning techniques," Sci. Rep. **12**, 4678 (2022).
[41]J. Chen, F. P. Brissette, and P. Lucas-Picher, "Assessing the limits of bias-correcting climate model outputs for climate change impact studies," J. Geophys. Res.: Atmos. **120**, 1123–1136, https://doi.org/10.1002/2014JD022635 (2015).
[42]M. Ashfaq, C. B. Skinner, and N. S. Diffenbaugh, "Influence of SST biases on future climate change projections," Clim. Dyn. **36**, 1303–1319 (2011).
[43]Y. H. Song and E.-S. Chung, "Intercomparison of bias correction methods for precipitation of multiple GCMs across six continents," Geosci. Model Dev. Discuss. **2024**, 1–55.
[44]T. Liu, X. Zhu, M. Tang, C. Guo, and D. Lu, "Multi-model ensemble bias-corrected precipitation dataset and its application in identification of drought-flood abrupt alternation in China," Atmos. Res. **307**, 107481 (2024).
[45]H. Li, J. Sheffield, and E. F. Wood, "Bias correction of monthly precipitation and temperature fields from Intergovernmental Panel on Climate Change AR4 models using equidistant quantile matching," J. Geophys. Res. **115**, D10101 (2010).
[46]H. A. Panofsky and G. W. Brier, *Some Applications of Statistics to Meteorology* (Mineral Industries Extension Services, College of Mineral Industries, Pennsylvania State University, 1968).
[47]S.-H. Kim, J. Hwang, and A. Sankarasubramanian, "Understanding the variability of large-scale statistical downscaling methods under different climate regimes," J. Hydrol. **641**, 131818 (2024).
[48]A. C. Bovik, *Basic Gray Level Image Processing. The Essential Guide to Image Processing* (Elsevier, 2009), pp. 43–68.
[49]N. Q. Minh, N. T. T. Huong, P. Q. Khanh, L. P. Hien, and D. T. Bui, "Impacts of resampling and downscaling digital elevation model and its morphometric factors: A comparison of Hopfield neural network, bilinear, bicubic, and kriging interpolations," Remote Sens. **16**, 819 (2024).
[50]Y. Chang, J. Wang, S. Li, and P. Chan, "A comprehensive review on the modeling of tropical cyclone boundary layer wind field," Phys. Fluids **36**, 035165 (2024).
[51]G. N. Walton, *Thermal Analysis Research Program Reference Manual: US Department of Commerce* (National Bureau of Standards, Washington, DC, 1983).
[52]L. Guan, "Preparation of future weather data to study the impact of climate change on buildings," Build. Environ. **44**, 793–800 (2009).
[53]H. Li, Y. Huo, Y. Fu, Y. Yang, and L. Yang, "Improvement of methods of obtaining urban TMY and application for building energy consumption simulation," Energy Build. **295**, 113300 (2023).
[54]Y. X. Ma and C. Yu, "Impact of meteorological factors on high-rise office building energy consumption in Hong Kong: From a spatiotemporal perspective," Energy Build. **228**, 110468 (2020).
[55]H. Li, T. Zhang, A. Wang, M. Wang, J. Huang, and Y. Hu, "A new method of generating extreme building energy year and its application," Energy **278**, 128020 (2023).
[56]S. Wilcox, "Users manual for TMY3 data sets," Technical Report NREL/TP-581-43156 (2008).
[57]K. E. Taylor, "Summarizing multiple aspects of model performance in a single diagram," J. Geophys. Res. **106**, 7183–7192, https://doi.org/10.1029/2000JD900719 (2001).
[58]U. S. Perera, M. Tharaka, A. Weerasuriya, C. Lewangamage, R. Ruparathna, and R. Mallawaarachchi, "Suitable passive design strategies for residential high-rise buildings in Sri Lanka," in *2023 Moratuwa Engineering Research Conference (MERCon)* (IEEE, 2023), pp. 101–106.